The International Journal of Advanced Manufacturing Technology (2018) 98:2775–2789
https://doi.org/10.1007/s00170-018-2457-0

ORIGINAL ARTICLE

Force prediction model considering material removal mechanism for axial ultrasonic vibration-assisted peripheral grinding of Zerodur

Guoyan Sun[1,2] · Lingling Zhao[3] · Zhen Ma[1] · Qingliang Zhao[4]

Received: 28 February 2018 / Accepted: 17 July 2018 / Published online: 24 July 2018

Abstract
Axial ultrasonic vibration-assisted peripheral grinding (AUPG) has the major advantages of simultaneously improving the grinding quality and material removal rate compared with conventional grinding methods. In this study, a grinding force prediction model for the AUPG of Zerodur was developed to investigate the generation mechanism of the grinding force for guidance in practical engineering applications. Taking into consideration the material removal mechanism, material properties and vibration impact, the three primary grinding force components were first separately modelled, namely, the ductile removal force in the ductile removal phase, the brittle removal force in the brittle removal phase and the frictional force of the friction process. The critical uncut chip thickness and maximum uncut chip thickness were subsequently researched to define the two material removal modes in the AUPG of Zerodur, namely, the ductile removal mode and the mixture of brittle and ductile removal mode. The grinding force models of these two material removal modes were developed using effective grinding force component models. The instantaneous variation of the grinding force with time and space was also analysed to derive models of the final time-averaged normal force, tangential force and axial force. Finally, grinding experiments were performed, the results of which showed that the prediction errors of the developed model were only 7.37 and 11.53% for the normal and tangential grinding forces, respectively. The axial ultrasonic vibration was also determined to reduce the surface roughness by 18.0% compared with conventional grinding, while the normal and tangential forces were reduced by 27.31 and 22.52%, respectively. This indicates that AUPG affords a significantly improved grinding surface quality. The developed model enables an understanding of the comprehensive mechanism of AUPG and provides a basis for the development of the grinding force models of the other brittle materials.

Keywords Grinding force model · Ultrasonic vibration · Zerodur · Brittle material · Brittle–ductile transition · Material removal mechanism

1 Introduction

Zerodur is a homogeneous microcrystalline glass characterised by an ultra-low coefficient of thermal expansion. It has several other desirable properties such as chemical inertness, thermal stability, good wear resistance and high hardness and strength. These properties give the material several potential applications including in space reflectors, inertial navigation, photoelectric measurement and precision machinery. However, conventional machining methods have technological limitations that make them incapable of achieving sufficient machining quality and high production efficiency required for the processing of Zerodur [1].

Ultrasonic vibration-assisted grinding (UVG) combines conventional grinding (CG) and ultrasonic vibration (UV). Numerous experimental and theoretical investigations have considered UVG to be an effective method for processing hard-brittle materials. Previous relevant studies have primarily focused on elliptical UV-assisted grinding (EUAG), axial UV-assisted peripheral grinding (AUPG) and axial UV-assisted

✉ Guoyan Sun
sunguoyan@opt.ac.cn

[1] Chinese Academy of Sciences, Xi'an Institute of Optics and Precision Mechanics, NO. 17 Xin xi Road, Xi'an 710119, People's Republic of China

[2] University of Chinese Academy of Sciences, Beijing 100049, China

[3] School of Mechanical Engineering, Shandong University of Technology, Zibo 255000, China

[4] Center for Precision Engineering School of Mechatronics Engineering, Harbin Institute of Technology, Harbin 150001, China

end grinding (AUEG), which are variously based on the different modulation directions of UV (see Figs. 1 and 2). Compared with EUAG, in which the workpiece is vibrated, AUEG and AUPG, which involve the vibration of the grinding wheels, enable the machining of optical components with large apertures. Although AUEG affords a high processing efficiency while decreasing the grinding force, it also leads to high surface roughness and subsurface damage [2, 3]. Conversely, AUPG has comprehensive advantages in improving surface/subsurface quality [4–6] and material removal rate [4], reducing grinding force [4, 5, 7–9], decreasing thermal load [6, 7] and inhibiting tool wear [8, 9]. AUPG thus has a wider range of potential applications in processing hard and brittle materials, for which reason it was the focus of the present study.

The grinding force is a key factor of AUPG, which influences the machine vibration, tool wear, grinding temperature and quality. Qin et al. [10] assumed that brittle fracture was the dominant material removal mode and derived a force model for the AUEG of silicon using the maximum indentation depth of a single-diamond grit in the workpiece based on the Hertz equation. Similar models were developed by Li et al. [11] for alumina, integrating the Vickers indentation theory; by Liu et al. [12] for carbon fibre reinforced plastic, based on the brittle fracture theory; and by Zhang et al. [13] for K9 optical glass, based on the indentation fracture mechanism. In addition, Xiao et al. [14] proposed a theoretical grinding force model for calculating the number of active abrasive grits in the feed and axial directions for zirconia ceramics. The foregoing previous studies primarily focused on the grinding force component vertical to the machining surface and considered only the brittle removal phase while neglecting the ductile removal stage, friction process and grinding force components in other directions. Zhang et al. [15] divided the material removal region in AUEG into the sliding grinding, ploughing grinding and main grinding regions and developed a radial force model, normal force model and tangential force model for silica glass and Al_2O_3 ceramic.

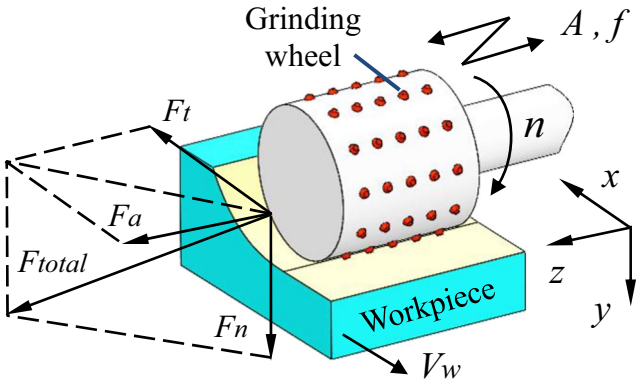

Fig. 2 Schematic illustration of the grinding force in AUPG

However, the modelling of the grinding force of AUPG has received less attention compared with that of AUEG, with the two processes characterised by differing relative movement between the workpiece and the grinding wheel. Based on a scratch test and indentation fracture mechanics, Li et al. [16] developed models of the tangential and normal forces of the AUPG of SiC ceramics, considering only the brittle fracture force. Zhou and Zheng [17] presented a force prediction model of the AUPG of SiCp/Al composites, considering the frictional force of the friction process, fracture force for the removal of SiCp ceramic particles and chip formation force for the removal of Al matrix, respectively. Xiao et al. [18] proposed a mathematical model of the grinding force in the ductile and brittle regions for the AUPG of zirconia ceramics, considering the brittle–ductile transition removal mechanism. However, the effect of friction on grinding force was not taken into consideration, and only the resultant force was analysed, without consideration of further development in instantaneous time and three-dimensional space. Kumar and Hutchings [19] reported that UV can be used to considerably reduce sliding friction. The effect of vibration input on friction reduction was also quantitatively examined by Tsai and Tseng [20]. Previous work is clearly insufficient for use in deriving an exact grinding force model for the AUPG of brittle materials, because such would involve a combination of an accurate trace of

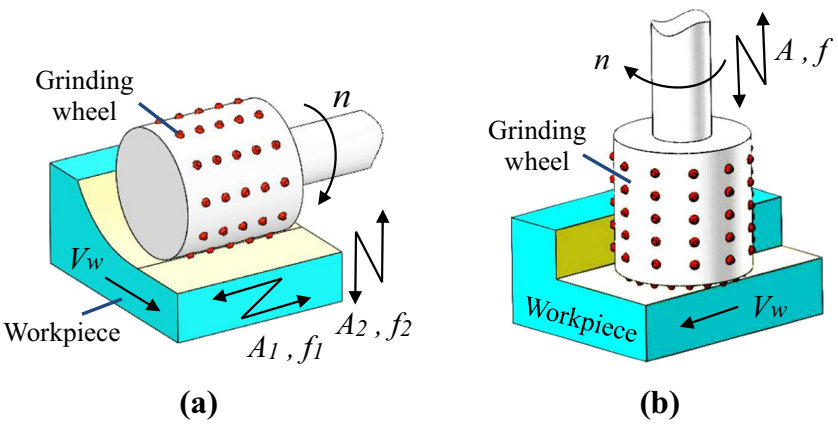

Fig. 1 Schematic illustrations of **a** EUAG and **b** AUEG

the material removal behaviour and the instantaneous change in time and space. Currently, there has been no quantitative investigation on the effect of vibration on the grinding force for the AUPG.

The present study explored the mechanism of the ductile/brittle material removal behaviour, the brittle–ductile transition threshold and the rubbing process, combining the effect of the axial vibration in the AUPG of Zerodur. A ductile removal force component model, a brittle removal force component model and a frictional force component model were established by adopting relevant original models. Further, through a kinematic analysis of the interference between the workpiece and a single abrasive grain, the instantaneous and average force models of the normal and tangential grinding forces were developed. Finally, the proposed grinding force model is capable of predicting the quantitative value and variation tendency of the grinding force with the input parameters for the AUPG of Zerodur and serving as a basis for the development of the grinding force models for the AUPG of other brittle materials.

Nomenclature

N_d	number of active diamond grit	b,a_e	grinding width and depth
V_w	feed rate of workpiece	l_g	geometric contact length
n	spindle speed of grinding wheel	H	workpiece material hardness
t	processing time	ξ	geometrical factor of indenter
t_c	effective contact time during a rotation period	C	abrasive concentration of grinding wheel
θ,d_s	semi-apex angle and diameter of single abrasive grain	R, d_e	equivalent radius and diameter of grinding wheel
$S_p(t)$,$S_c(t)$	motion of single diamond grit in AUPG and CG	$V_p(t)$,$V_c(t)$	velocity of single diamond grit in AUPG and CG
l_p,l_c	dynamic contact length in AUPG and CG	a_{pmax},a_{gmax}	maximum uncut chip thickness in AUPG and CG
E_1,E_2	elastic modulus of workpiece material and diamond grit material	ν_1,ν_2	Poisson's ratio of workpiece material and diamond grit material
E_1^*	elastic modulus of workpiece material in AUPG	ω,V_s	angular velocity and circular velocity of diamond grit
K_{ID},K_{IC}	dynamic and static fracture toughness of workpiece material	A,f	vibration amplitude and frequency
$\overline{a_{gd1}}$	average cutting depth of ductile removal mode in AUPG	$\overline{a_{gd2}}$	average cutting depth in ductile removal phase in AUPG
F_b	average brittle removal force	a_{gc}	critical uncut chip thickness
F_p	grinding force per unit area in ductile region	δ	real contact area between single diamond grit and workpiece
F_{max}	maximum contact force	α_V	top angle of Vickers indenter
p_0	empirical proportionality constant to frictional force	α, β	material coefficients of friction pairs
λ_0	integrative factor	γ	friction reduction ratio by UV
F_{dn},F_{dta}	ductile removal normal force and tangential force	F_{bn},F_{bta}	normal force and tangential force in brittle removal mode
F_{fn},F_{fta}	normal and tangential frictional force	F_n,F_t,F_a	final normal, tangential and axial force

2 Development of grinding force model

The grinding of Zerodur is a complex process which contains elastic deformation, plastic ploughing, micro/macro cracking, micro/macro fracturing and rubbing. The establishment of models of the grinding force components induced by ductile material removal, brittle material removal and the friction behaviour thus necessitates a comprehensive analysis of the material removal mechanism. The total grinding force F_{total}, normal grinding force F_n, tangential grinding force F_t and axial grinding force F_a of AUPG are illustrated in Fig. 2 in a rectangular coordinate system. When ultrasonic oscillation is superimposed on conventional spindle rotation in AUPG, the primary constant cutting velocity generated by the spindle rotation is modulated by the periodic vibration action. The grinding trajectory overlap ratio, material properties, material removal mode and friction process are also affected to different degrees. Consideration of these parameters is thus critical to the development of the grinding force model for AUPG.

Grinding can be regarded as a complex cutting action involving numerous single abrasive grains. The grinding force of a single abrasive grain is used as an investigation unit for obtaining a macroscopic grinding force model. The number of active diamond grits, N_d, is another essential parameter and can be expressed as

$$N_d = bCl_g \tag{1}$$

The following assumptions and simplifications are adopted:

1. An abrasive grit is a rigid cone with semi-apex angle θ, as shown in Fig. 3.

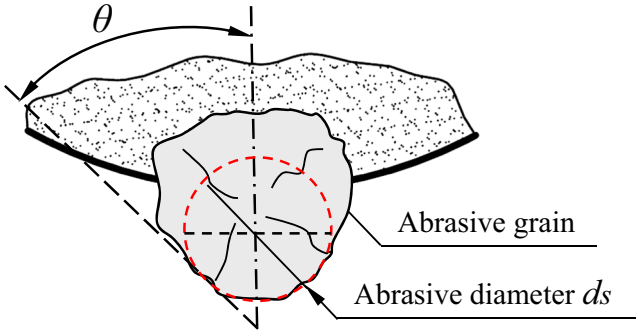

Fig. 3 Schematic of an abrasive grain

2. The machining process is stable with a constant vibration amplitude A and frequency f.
3. Cooling of the grinding process is not considered in the grinding force model.

2.1 Process kinematics and geometry of single-diamond grit

The movement of a single abrasive grain relative to the workpiece, including the rotational circular spindle motion axial UV, and the horizontal feed movement of the workpiece are shown in Fig. 2. The kinematic motion and velocity of a single abrasive grain for AUPG and CG are, respectively, expressed as

$$S_p(t)=\begin{pmatrix}S_x(t)\\S_y(t)\\S_z(t)\end{pmatrix}=\begin{pmatrix}V_w t+R\sin(\omega t)\\-R\cos(\omega t)\\A\sin(2\pi ft)\end{pmatrix}=\begin{pmatrix}S_x(t)\\S_y(t)\end{pmatrix}=S_c(t) \tag{2}$$

$$V_p(t)=\begin{pmatrix}V_x(t)\\V_y(t)\\V_z(t)\end{pmatrix}=\begin{pmatrix}V_w+R\omega\cos(\omega t)\\R\omega\sin(\omega t)\\2A\pi f\cos(2\pi ft)\end{pmatrix}=\begin{pmatrix}V_x(t)\\V_y(t)\end{pmatrix}=V_c(t) \tag{3}$$

Figure 4 shows the geometric contact length l_g [8] and dynamic contact length l_c for CG and the dynamic contact length l_p for AUPG. These parameters can be, respectively, expressed as

$$l_g\approx\sqrt{a_e d_e} \tag{4}$$

$$l_c=\int_0^{t_c}\sqrt{V_x(t)^2+V_y(t)^2}\,dt\approx l_g \tag{5}$$

$$l_p=\int_0^{t_c}V_P dt\approx\int_0^{t_c}\sqrt{(\pi n d_e)^2+(2A\pi f\cos(2\pi ft))^2}\,dt \tag{6}$$

where t_c is the effective contact time of the abrasive grit as it penetrates the workpiece during a rotation period, given by

$$t_c=l_g/V_s \tag{7}$$

A comparison of Eqs. (5) and (6) reveals that l_p is longer than l_c, with the exact difference between them entirely determined by the vibration amplitude and frequency.

As shown in Fig. 5, the material removal process of the AUPG of Zerodur can be divided into ductile and brittle phases. The critical uncut chip thickness a_{gc} of the brittle–ductile transition and the maximum uncut chip thickness a_{gmax} are, respectively, given by [21]

$$a_{gmax}=2\left[\frac{V_w}{V_s N_d m}\sqrt{\frac{a_e}{d_e}}\right]^{1/2} \tag{8}$$

$$a_{gc}=\cot\alpha_V\sqrt{\frac{2\lambda_0}{\xi}}\left(\frac{K_{ID}}{H}\right)^2 \tag{9}$$

$$K_{ID}\approx 0.3K_{IC} \tag{10}$$

When a_{gmax} is smaller than a_{gc}, the removal of the material is entirely in the ductile mode. The material removal becomes a mixture of the brittle and ductile mode when a_{gmax} exceeds a_{gc}.

2.2 Probability of two material removal modes

Considering the differing protrusion heights of the abrasive grains in the grinding wheel, the uncut chip thickness a_g can be described using the Raleigh probability function [22], which is expressed as

$$f(a_g)=\begin{cases}\left(\frac{a_g}{\sigma^2}\right)e^{\frac{-a_g}{2\sigma^2}} & a_g\geq 0\\ 0 & a_g<0\end{cases} \tag{11}$$

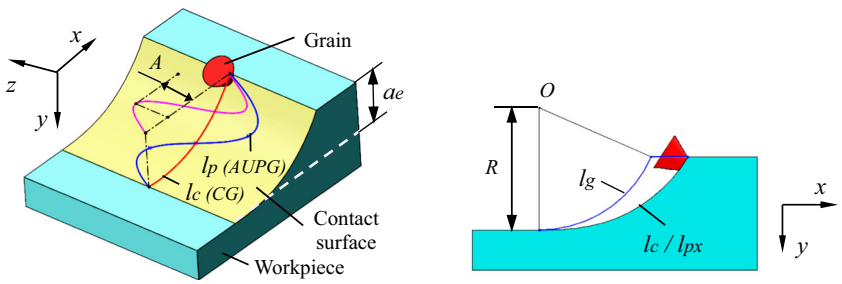

Fig. 4 Motion trajectories of an abrasive grit in AUPG and CG

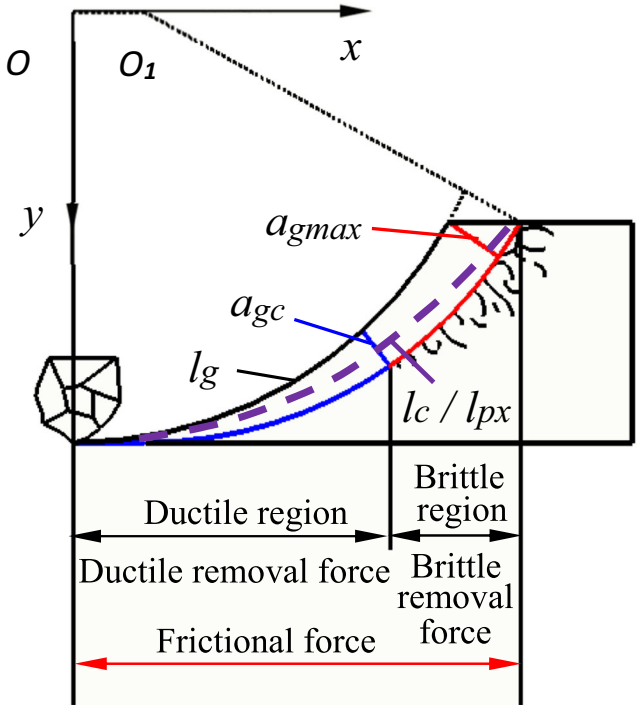

Fig. 5 Geometry of a brittle material removal process

As shown in Fig. 6, the brittle material removal by the abrasive grains occurs in the areas where a_g over a_{gc}, while ductile material removal occurs where a_g below a_{gc}. By integrating the uncut chip thickness probability density function $f(a_g)$, the occurrence probability of the ductile material removal mode δ_1 is given by

$$\delta_1 = \int_0^{a_{gc}} f(a_g)\, da_g = 1 - e^{\frac{-a_{gc}}{2\sigma^2}} \tag{12}$$

Accordingly, the occurrence probability of the combination of the brittle and ductile modes δ_2 is given by

$$\delta_2 = 1 - \delta_1 \tag{13}$$

The ductile removal behaviour is exhibited in both the ductile removal mode and the mixture of brittle and ductile removal mode. Therefore, the probability of the abrasive grains engaged in the ductile removal behaviour is $\delta_1 + \delta_2 = 1$. Conversely, the brittle removal behaviour only occurs in the mixture of brittle and ductile removal mode, and its probability is therefore δ_2.

The defining parameter σ of the Raleigh probability function can be related to the grinding parameters through the equal material removal volume [23]. The parameter σ_c for CG and σ_p for AUPG can be, respectively, established as Eqs. (14) and (15), respectively.

$$\sigma_c = \sqrt{\frac{a_e V_w}{2 V_s C l_c \tan\theta}} \tag{14}$$

$$\sigma_p = \sqrt{\frac{a_e V_w}{2 V_s C l_p \tan\theta}} \tag{15}$$

By substituting Eqs. (14) and (15) into Eq. (12), the probability of the ductile material removal mode for CG can be determined to less than that for AUPG, considering that $l_c < l_p$ according to Eqs. (5) and 6). It can thus be concluded that the axial ultrasonic vibration parallel to the ground surface increases the probability of the ductile material removal mode.

2.3 Ductile removal force model for AUPG

When the material is removed solely by elastoplastic deformation, the average cutting depth $\overline{a_{gd1}}$ can be calculated using Rayleigh's probability density function [3, 6]:

$$\overline{a_{gd1}} = \sqrt{\frac{\pi a_e V_w}{4 C l_p V_s \tan\theta}} \qquad a_{gmax} \le a_{gc} \tag{16}$$

When the material is removed by both elastic–plastic deformation and brittle fracturing, the average cutting depth $\overline{a_{gd2}}$ in the ductile removal phase can be related to a_{gc} through the equivalent removal volume, as shown in Fig. 7.

$$\overline{a_{gd2}}^2 \tan\frac{\theta}{2} l_p = \frac{1}{3} a_{gc}^2 \tan\frac{\theta}{2} l_c \tag{17}$$

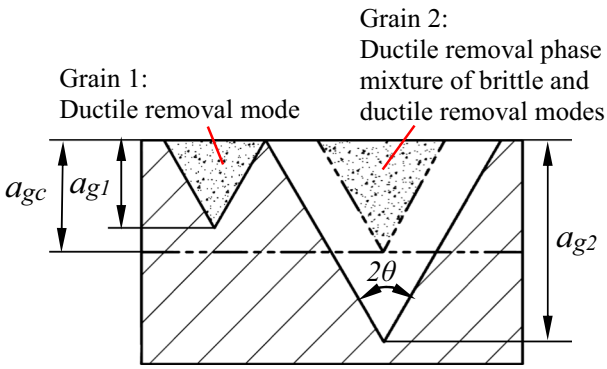

Fig. 6 Theoretical profiles of the grooves generated by an abrasive grain

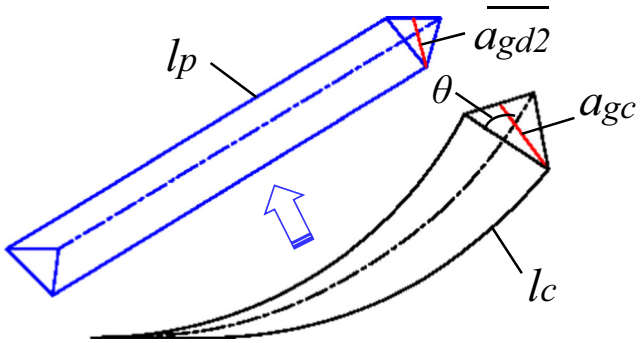

Fig. 7 Calculation of the average cutting depth in the ductile removal phase

$$\overline{a_{gd2}} = \sqrt{\frac{l_c}{3l_p}}\, a_{gc} \approx \sqrt{\frac{l_g}{3l_p}}\, a_{gc} \qquad a_{gmax} > a_{gc} \tag{18}$$

The average plastic removal cutting depth for AUPG is clearly smaller than that for CG, because of the longer dynamic contact length l_p. Figure 8 shows the normal force component F_n and the horizontal force component F_{ta} in a rectangular coordinate system. The chip formation force models for mild steel [24] and SiCp/Al composite [17] can be used to establish the ductile removal force model for Zerodur, owing to their similar plastic flow removal mechanisms. The ductile removal force generated by a single abrasive grit is regarded as the integral of the grinding force per unit area F_p over the contact area between the single abrasive grit and the workpiece. The normal and horizontal force components of the ductile removal force can thus be calculated based on the number of effective diamond gritsN_d, as follows [17, 24]:

$$F_{dn} = N_d F_p \overline{a_{gd}}^{\,2} \sin\theta\tan\theta \tag{19}$$

$$F_{dta} = \frac{\pi}{4} N_d F_p \overline{a_{gd}}^{\,2} \sin\theta \tag{20}$$

When $a_{gmax} \le a_{gc}$, by setting $k_1 = \frac{F_p \sin\theta}{4}$ and $k_2 = \frac{\pi F_p \cos\theta}{16}$, then substituting Eq. (16) into Eqs. (19) and (20), we obtain

$$F_{dn1} = k_1 \frac{b}{l_p {d_e}^{1/2}} \frac{V_w}{n} {a_e}^{3/2} \tag{21}$$

$$F_{dta1} = k_2 \frac{b}{l_p {d_e}^{1/2}} \frac{V_w}{n} {a_e}^{3/2} \tag{22}$$

When $a_{gmax} > a_{gc}$, by setting $k_3 = \frac{F_p \sin\theta\tan\theta}{3}$ and $k_4 = \frac{\pi F_p \sin\theta}{12}$, then substituting Eq. (18) into Eqs. (19) and (20), we obtain

$$F_{dn2} = k_3 \frac{b c d_e {a_{gc}}^2}{l_P} a_e \tag{23}$$

$$F_{dta2} = k_4 \frac{b c d_e {a_{gc}}^2}{l_P} a_e \tag{24}$$

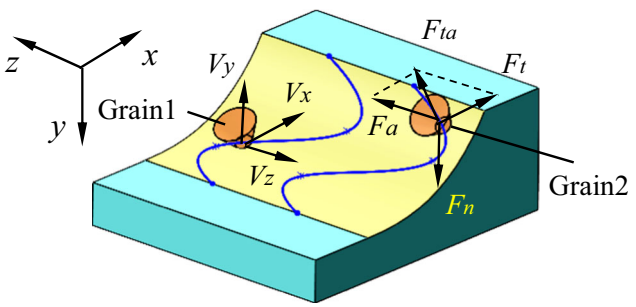

Fig. 8 Illustration of the grinding force in AUPG

2.4 Brittle removal force model for AUPG

Cracking and fracturing are the primary material removal methods in the brittle removal region. Cutting force models for the AUEG of brittle materials have been previously developed, considering only brittle fracturing as the dominant material removal mode [10, 13]. This approach is also appropriate for modelling the brittle removal force for Zerodur in the brittle removal phase. In the procedure, the impulse theorem is used to relate the brittle removal force to the maximum contact force F_{max}, which can be calculated based on the maximum indentation depth a_{pmax} using the Hertz equation, as expressed by Eqs. (25) and (26).

$$F_b = N_d F_{max} t_c n \tag{25}$$

$$F_{max} = \left(\frac{8}{9}\left(\frac{{E_1}^*}{1-{\nu_1}^2}\right)^2 d_s {a_{pmax}}^3\right)^{1/2} = \frac{2\sqrt{2}}{3}\frac{{E_1}^*}{1-{\nu_1}^2} {d_s}^{1/2} {a_{pmax}}^{3/2} \tag{26}$$

In AUPG, the maximum cutting depth a_{pmax} is a key factor in modelling the fracturing force. Assuming that the geometric volumes of the single-diamond grits for AUPG and CG are equal, a_{pmax} can be related to a_{gmax}, as shown in Fig. 9.

$$\frac{1}{3}{a_{pmax}}^2 \tan\frac{\theta}{2} l_p = \frac{1}{3}{a_{gmax}}^2 \tan\frac{\theta}{2} l_c \tag{27}$$

$$a_{pmax} = \sqrt{\frac{l_c}{l_p}}\, a_{gmax} \approx \sqrt{\frac{l_g}{l_p}}\, a_{gmax} \tag{28}$$

The application of the impact force on the workpiece alters the material properties of the latter, including changing the internal stress state and initiating cracking. Through a Hopkinson pressure bar test, Lv [2] demonstrated that the elastic modulus of BK7 was affected by the loading velocity. The elastic modulus ${E_1}^*$ of the workpiece material during AUPG is thus assumed to be proportional to the elastic modulus E_1 during CG:

$${E_1}^* = K_e E_1 \tag{29}$$

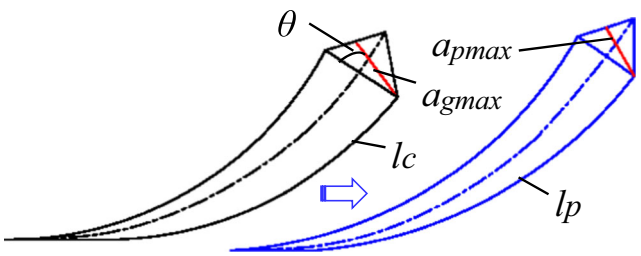

Fig. 9 Calculation parameters of the maximum cutting depth in the ductile removal phase

The initiation of cracks in Zerodur in the ductile removal phase strongly depends on the material hardness and dynamic fracture toughness. A nano-indentation test (Nano-Indenter XP) and micro-hardness indentation test (HVS-1000Z) were thus conducted in the present study to determine the elastic modulus, hardness and dynamic fracture toughness of Zerodur. The measured and calculated material properties are presented in Table 1. The calculations were based on the indentation feature size.

The relationship between the elastic modulus and the hardness and dynamic fracture toughness of Zerodur, as determined from the results of the indentation test, is as follows:

$$E_1 = 7193.43\frac{{K_{ID}}^2}{H} \tag{30}$$

Substituting Eq. (26) and Eqs. (28)–(30) into Eq. (25), then setting k_5 and $k_6 \propto \frac{19182.48K_e}{\pi^{7/4}m^{3/4}}$, the normal and horizontal components of the brittle removal force can be, respectively, expressed as

$$F_{bn} = k_5\frac{{d_s}^{1/2}}{1-{\nu_1}^2}\frac{{K_{ID}}^2}{H}\frac{(bc)^{1/4}}{{d_e}^{9/8}{l_p}^{3/4}}\left(\frac{V_w}{n}\right)^{3/4}{a_e}^{11/8} \tag{31}$$

$$F_{bta} = k_6\frac{{d_s}^{1/2}}{1-{\nu_1}^2}\frac{{K_{ID}}^2}{H}\frac{(bc)^{1/4}}{{d_e}^{9/8}{l_p}^{3/4}}\left(\frac{V_w}{n}\right)^{3/4}{a_e}^{11/8} \tag{32}$$

2.5 Frictional force model for AUPG

The frictional force between the workpiece surface and the abrasive grains in the work plane for CG was established in a former study based on the frictional binominal theorem [24] and can be expressed as follows:

$$F_{cfn} = N_d\delta\overline{p} \tag{33}$$

$$F_{cfta} = \mu N_d\delta\overline{p} \tag{34}$$

Table 1 Mechanical properties of Zerodur

Property	Value
Elastic modulusE_1 (Gpa)	87.89
Poisson ratio ν_1	0.240
Vickers hardness H (Gpa)	7.062
Static fracture toughness K_{IC}(Mpa · $m^{1/2}$)	0.979
Dynamic fracture toughness K_{ID}(Mpa · $m^{1/2}$)	0.294
Critical uncut chip thickness a_{gc}(μm)	0.055

The average contact pressure between the workpiece and a single abrasive grain,$\overline{p}$, can be derived linearly in terms of the empirical proportionality constant of the frictional force p_0, as follows [17]:

$$\overline{p} = \frac{4p_0V_w}{d_eV_s} \tag{35}$$

Furthermore, the frictional coefficientμ is determined by the average contact pressure$\overline{p}$, based on the frictional binomial theorem [17]:

$$\mu = \frac{\alpha}{\overline{p}} + \beta \tag{36}$$

By substituting Eqs. (35) and (36) into Eqs. (33) and (34), the total normal and tangential frictional forces can, respectively, be expressed as

$$F_{cfn} = \frac{4\delta p_0}{\pi}\frac{bc}{{d_e}^{3/2}}\frac{V_w}{n}{a_e}^{1/2} \tag{37}$$

$$F_{cfta} = \alpha\delta bc{a_e}^{1/2}{d_e}^{1/2} + \frac{4\beta\delta p_0}{\pi}\frac{bc}{{d_e}^{3/2}}\frac{V_w}{n}{a_e}^{1/2} \tag{38}$$

The application of vibration significantly reduces the frictional force, as observed in previous experiments [19, 20]. Tsai developed a theoretical approach for analysing the specific effect of tangential vibration at an arbitrary angle on friction reduction [20]. As illustrated in Fig. 10, the vibration in AUPG is vertical to the grain macroscopic velocity in CG. Accordingly, the friction reduction ratio can be calculated explicitly as follows:

$$\gamma = \frac{2}{\pi}\frac{\varepsilon}{\sqrt{1+\varepsilon^2}}K\left(\frac{1}{1+\varepsilon^2}\right) \tag{39}$$

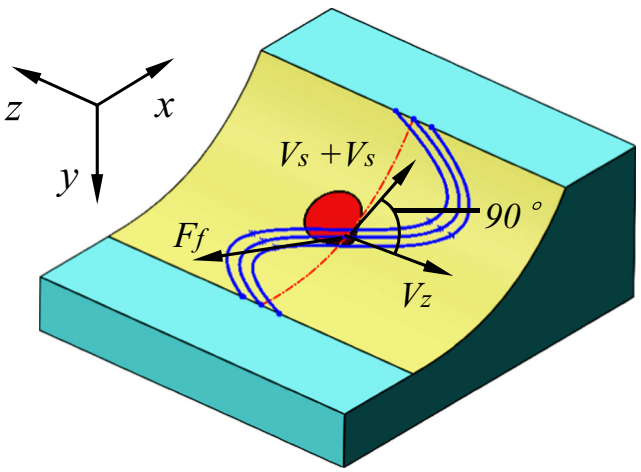

Fig. 10 Illustration of the frictional force in AUPG

where $K(\varepsilon)$ is the complete elliptic integral of the first kind, and ε is the ratio of the constant grain macroscopic velocity to the amplitude of the harmonic vibration velocity.

$$\varepsilon = \frac{V_w + V_s}{V_z} = \frac{V_w + \pi n d_e}{2A\pi f} \tag{40}$$

Setting $k_7 = \frac{4\delta p_0}{\pi}$, $k_8 = \frac{2\alpha\delta}{\pi}$ and $k_9 = \frac{8\beta\delta p_0}{\pi^2}$, the normal and horizontal components of the frictional force can be, respectively, obtained as

$$F_{fn} = \gamma F_{cfn} = k_7\gamma \frac{bc}{{d_e}^{3/2}} \frac{V_w}{n} {a_e}^{1/2} \tag{41}$$

$$F_{fta} = \gamma F_{cfta} = k_8\gamma bc {a_e}^{1/2} {d_e}^{1/2} + k_9\gamma \frac{bc}{{d_e}^{3/2}} \frac{V_w}{n} {a_e}^{1/2} \tag{42}$$

2.6 Final grinding force model for AUPG

The direction and magnitude of the horizontal grinding force F_{ta} change periodically in conformity with the axial vibration, as shown in Fig. 11. The angle φ_d between the instantaneous horizontal grinding force F_{ta} and the X axis can be calculated as follows:

$$\varphi_d = \arctan\left(\frac{V_z(t)}{V_s}\right) = \arctan\left(\frac{2A\pi f \cos(2\pi f t)}{\pi n d_e}\right) \tag{43}$$

The horizontal grinding force in the XOZ plane can be geometrically divided into two components. The first component is along the X axis and is defined as the tangential grinding force. The second component is along the Z axis and is defined as the axial grinding force. The time-averaged tangential grinding force F_t and axial grinding force F_a can be calculated using the following calculus equations:

$$F_t = \frac{F_{ta}}{\varphi_{dmax}} \int_0^{\varphi_{dmax}} \cos\varphi_d d\varphi_d = K_{\varphi_{dmax}} F_{ta} \tag{44}$$

where $K_{\varphi_d} = \frac{1}{\varphi_{dmax}} \int_0^{\varphi_{dmax}} \cos\varphi_d d\varphi_d$, and $\varphi_{dmax} = \arctan\left(\frac{AW_f}{\pi n d_e}\right)$.

$$F_a = \frac{F_{ta}}{\varphi_{dmax}} \int_0^{\varphi_{dmax}} \sin\varphi_d d\varphi_d \approx 0 \tag{45}$$

It can be deduced from Fig. 11 and Eqs. (44) and (45) that the magnitude of the tangential grinding force fluctuates during an oscillation period, whereas the magnitude and direction of the axial grinding force change periodically and is symmetric with the X axis. The average axial grinding force F_a during a vibration period is thus zero, while the average tangential grinding force F_t is less than F_{ta}.

Figure 12 shows the flowchart of the modelling of the grinding force in AUPG based on the material properties, grinding parameters and vibration parameters. When $a_{gmax} \le a_{gc}$, the grinding force is introduced by material elastoplastic deformation resistance and sliding friction between the abrasive grains and the workpiece. The grinding force is therefore composed of a frictional force component and a ductile removal force component.

$$F_n = F_{dn1} + F_{fn} \tag{46}$$

$$F_t = K_{\varphi_d}\left(F_{dta1} + F_{fta}\right) \tag{47}$$

When $a_{gmax} > a_{gc}$, the grinding force is obtained by adding the ductile removal force component in the ductile removal phase, the brittle removal force component in the brittle removal phase and the frictional component. By combining the grinding force components with the probability mentioned in Sect. 2.2 [25], the final grinding force can be modelled as follows:

$$F_n = F_{dn2} + \delta_2 F_{bn} + F_{fn} \tag{48}$$

$$F_t = K_{\varphi_d}\left(F_{dta2} + \delta_2 F_{bta} + F_{fta}\right) \tag{49}$$

The coefficients k_1–k_9 in Eqs. (46)–(49) can be determined by experiments, as described in the next section.

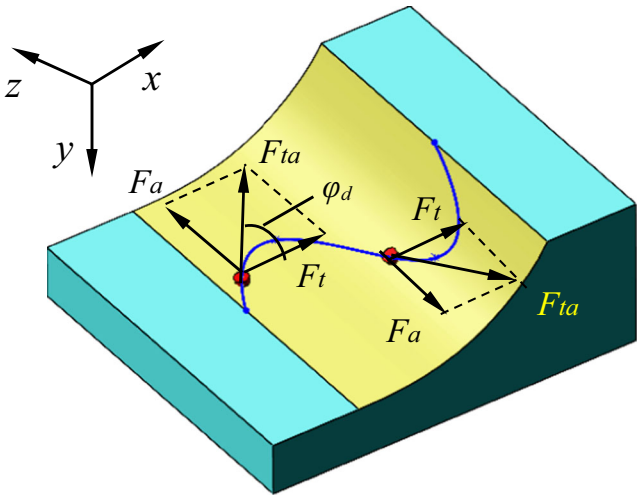

Fig. 11 Schematic of the tangential grinding force in AUPG

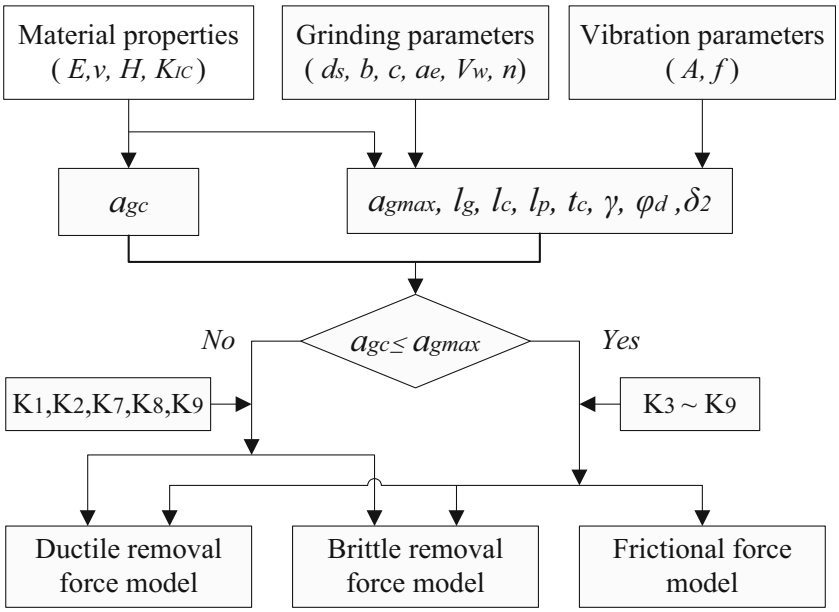

Fig. 12 Flowchart for modelling the grinding force of AUPG

3 Determination of proportionality coefficients

3.1 Experimental setup

The experiments were performed on a precision grinding machine (MUGK7120X5) with an ultrasonic air spindle system (DQFX-12040), as shown in Fig. 13. The variable speed spindle, capable of rotating at up to 20,000 rpm, was fixed on the *X* slide of the precision grinder. A vibrator was added to the spindle to generate an UV in the axial direction for AUPG. A vibration frequency of 23.67 kHz and amplitude of 11.20 μm were applied in the experiments. As illustrated in Fig. 14, the vibration amplitude and frequency of the grinding spindle were measured by a laser displacement sensor (Keyence LK-H020), which specifically monitored the diamond-turned end surface of an aluminium rod fixed on the grinding spindle. The workpiece was mounted on a dynamometer fixed on the *Z* slide of the precision grinder. The grinding forces were measured by a high-precision force dynamometer (Kistler 9256C) and surface roughness Ra by an atomic force microscope (Dimension 3100). The surface topography was observed by a scanning electron microscope (Zeiss Gemini500).

3.2 Experimental design and results

The mechanical properties of the Zerodur workpiece were obtained through a nano-indentation test, as presented in Table 1. As shown in Fig. 15, the dimensions of the Zerodur workpiece were 15 × 12 × 10 mm, with a prefabricated width of 3 mm to ensure that the grinding width of the samples of each group was exactly consistent. The specifications of the grinding wheel with resin-bonded mono-layer fine-grained diamond abrasives are presented in Table 2. The experiments of this study were designed for the purpose of deriving a grinding force model of the complex coexistence of the ductile and brittle material removal modes. The experimental conditions are detailed in Table 3. By substituting the parameters in the table into Eq. (8), the maximum uncut chip thickness a_{gmax} values were determined to be within 0.103–0.180 μm, which is greater than the critical uncut chip thickness a_{gc}, as indicated in Table 1.

The grinding forces determined by the experiments were substituted into Eqs. (48) and (49) and the coefficients k_3–k_9 were calculated, as presented in Table 4.

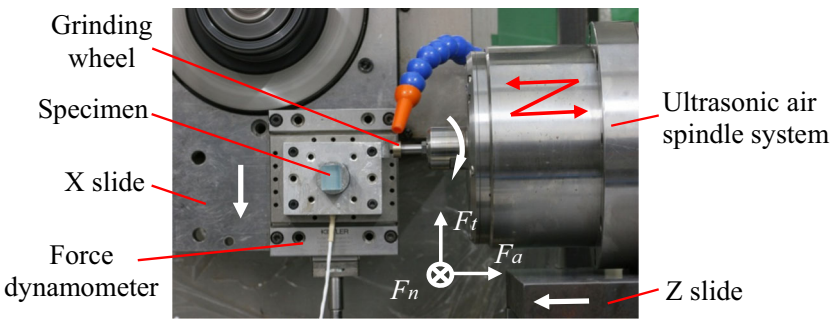

Fig. 13 Grinding experiment system

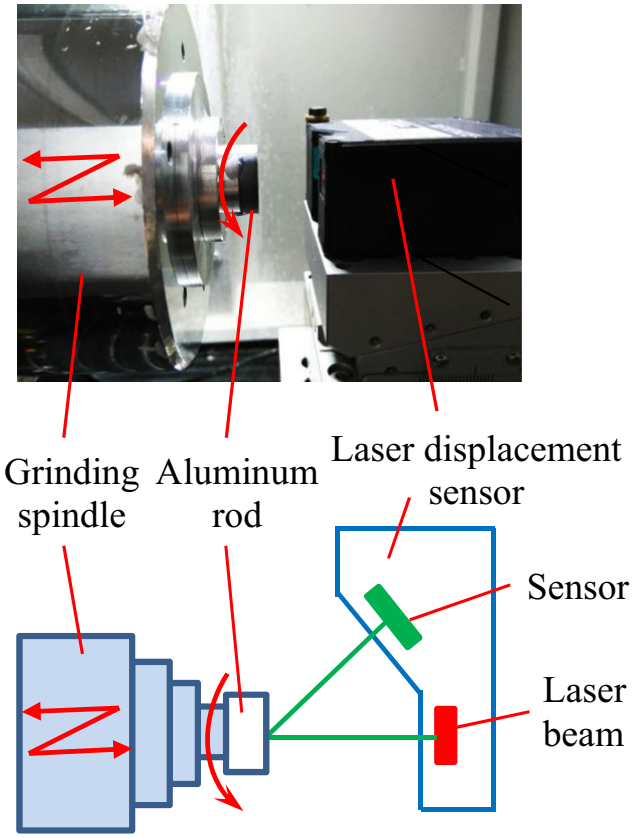

Fig. 14 Schematic of the setup for measuring the vibration amplitude and frequency of the grinding spindle

4 Experimental verification

Verification experiments were also performed to determine the deviation between the predictions of the proposed grinding force model and the experimental results and examine the effect of the UV on the grinding force. CG and AUPG experiments were performed under the same process conditions. The grinding parameters and calculated process variables are presented in Table 5.

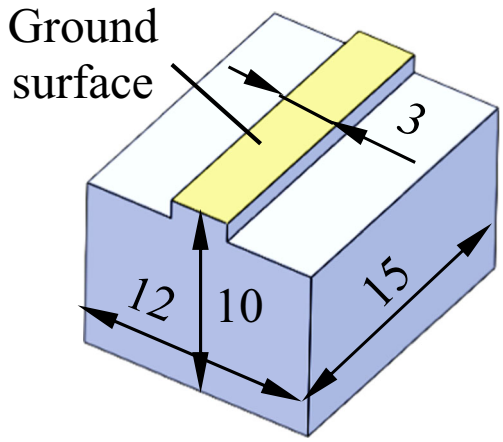

Fig. 15 Dimensions of the Zerodur workpiece

Table 2 Specifications of the diamond wheel used for the experiments

Parameter	Value
Diameter (mm)	12
Mesh size	D7
Abrasive size d_s(mm)	0.01
Abrasive concentration$C$	100
Abrasive elastic modulusE_2 (Gpa)	1141
Abrasive Poisson's ratio ν_2	0.07

The measured and predicted grinding forces are compared in Figs. 16 and 17, from which good quantitative and variation trend agreement can be observed for AUPG. The normal grinding force F_n and tangential grinding force F_t can be seen to increase significantly with increasing grinding depth and feed rate. This is primarily because of increases in the number of active diamond grits and the material volume removed by a single abrasive grain. Conversely, F_n and F_t decrease first but then grow up with increasing spindle speed. High spindle speed leads to higher radial runout of spindle, which directly influences the grinding force. The relative errors between the predicted and experimentally measured values of the normal grinding force and tangential grinding force are 7.37 and 11.53%, respectively. Moreover, the grinding forces for AUPG are considerably lower than those for CG (by 27.31% for F_n and 22.52% for F_t). This implies that the axial UV peripheral applied to the grinding surface in AUPG significantly reduces the grinding force. Based on Eqs. (5) and (6), the dynamic contact length l_p in AUPG is longer than the dynamic contact length l_c in CG, and this contributes to the reduction of the ductile and brittle removal force components of AUPG inferred by Eqs. (48) and (49). The vibration also significantly decreases the frictional force by a ratio of γ, as discussed in Sect. 2.5. The improvements of the grinding trajectory overlap ratio and the probability of the ductile material removal mode under UV also contribute to the decrease in the grinding force of AUPG.

Table 3 Experimental conditions used to determine the proportionality coefficients

V_s(mm/min)	V_wV$_w$(mm/min)	a_e(μm)
301,593, 376,991, 452,389, 527,788	5	7
376,991	5,7,9,11	7
376,991	5	4,7,10,13

Table 4 Coefficients used in the surface grinding force model

k_3	k_4	k_5	k_6	k_7	k_8	k_9
2.824×10^7	2.380×10^6	4.454×10^8	1691	2.870×10^4	0.011	1095

To quantitatively assess the material removal mechanism and the final surface quality afforded by each of CG and AUPG, Ra and the surface topography were further investigated. Figure 18 compares the surface roughness results of CG and AUPG. It can be seen that the axial UV parallel to the grinding surface considerably reduces Ra by an average of approximately 18.00%. In addition, the variation of Ra with the grinding parameters is similar to that of the grinding force, indicating that the grinding parameters can be optimised by the proposed grinding force model to achieve a higher machining efficiency and quality.

The surface characteristics after CG and AUPG using the same grinding parameters of the group 1 and group 8 experiments are, respectively, illustrated in Figs. 19 and 20. As can be observed from Fig. 19a, the final surface generated by CG in the group 1 experiments contains dense grinding waves with evident peaks and valleys parallel to the workpiece feed direction. There are two macro-fractures along the deepest groove, while small pits and micro-cracks are distributed mainly on the groove, with plastic ploughing also occurring mostly on the uplift, as shown in Fig. 19b. This shows that the CG of Zerodur is predominantly by plastic deformation and brittle fracturing. As illustrated in Fig. 19c, d, a higher surface quality is achieved by AUPG, as attested by the shallow grinding waves, uniform ploughing marks and less brittle fractures. Obviously, the superposition of UV onto CG can enlarge the ductile removal zone and reduce the surface damage. The foregoing comparative qualities of CG and AUPG can also be observed from Figs. 20a–d, although plastic ploughing and micro-fracturing are both primary material removal forms of CG and AUPG in the group 8 experiments. Through the comparison between Fig. 20a, c, the plastic ploughing region in CG is parallel to the brittle fracture region, while that in AUPG has an irregular shape. Moreover, the area of the plastic ploughing region in AUPG is larger than that in CG, and the depth of micro-fractures is shallower. As observed from Fig. 20b, d, grinding marks in the plastic ploughing zone generated by CG are more remarkable compared to AUPG which introduces additional axial vibration onto diamond grinding grains. It is evident from the above observations that the axial UV parallel to the grinding surface substantially enlarges the ductile material removal region, and thus significantly improves the grinding surface quality. The effects of the axial UV on the grinding surface can be summarised in three aspects: firstly, the overlap of the grain trajectory induced by the axial UV reduces the uncut chip thickness of a single-diamond grit, thereby decreasing the grinding force and surface/subsurface damage, and also reduces the irregularities in the height of the grinding surface, resulting in improved surface consistency. Secondly, Zerodur is more likely to be removed in the ductile mode during AUPG because the axial UV parallel to the ground surface enlarges the ductile cutting region in the brittle material, as attested by Wang et al. [1]. Equations (14) and (15) in Sect. 2.2 also indicate that the probability of the ductile material removal mode in AUPG is higher than that in CG, because $l_c < l_p$. Thirdly, the axial UV parallel to the grinding surface reduces the wear and fracture of the diamond abrasives, as reported by Peng et al. [26], resulting in enhanced surface quality and forming accuracy.

Table 5 Experimental conditions and process variables used for the verification of the grinding force model

Group	n (rpm)	V_w (mm/min)	a_e (μm)	Grinding method	l_p (mm)	γ	K_{φ_d}	δ_2
1	8000	5	8	CG and AUPG	0.3189	0.2211	0.9835	0.1514
2	12,000	5	8	CG and AUPG	0.3135	0.1293	0.9926	0.0618
3	16,000	5	8	CG and AUPG	0.3119	0.0842	0.9960	0.0249
4	20,000	5	8	CG and AUPG	0.3113	0.0593	0.9976	0.0100
5	12,000	10	8	CG and AUPG	0.3135	0.1293	0.9926	0.2486
6	12,000	15	8	CG and AUPG	0.3135	0.1293	0.9926	0.3954
7	12,000	20	8	CG and AUPG	0.3135	0.1293	0.9926	0.4986
8	12,000	5	5	CG and AUPG	0.2477	0.1293	0.9926	0.0296
9	12,000	5	11	CG and AUPG	0.3678	0.1293	0.9926	0.0930
10	12,000	5	14	CG and AUPG	0.4145	0.1293	0.9926	0.1220

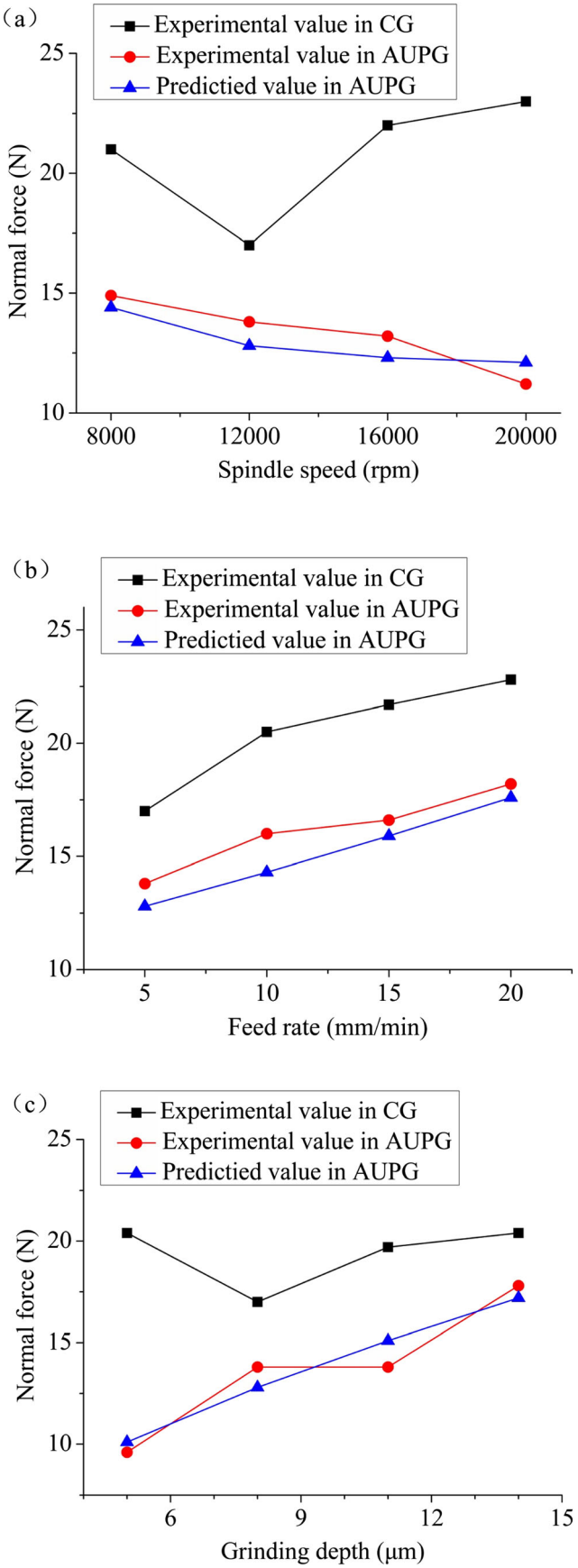

◀ **Fig. 16** Predicted and measured normal grinding forces for **a** $a_e = 8$ μm, $v_w = 5$ mm; **b** $a_e = 8$ μm, $n = 10{,}000$ rpm; and **c** $v_w = 5$ mm, $n = 10{,}000$ rpm

Furthermore, the surface quality achieved by the group 8 experiments is obviously superior to that of the group 1 experiments, as evidenced by the shallower surface waves and flatter overall surface. The decreased grinding depth and increased spindle speed contribute to the improvements of the group 8 experiments by reducing the uncut chip thickness determined by Eqs. (16), (18), and (28), as well as increasing the probability of the ductile material removal mode calculated by Eqs. (14) and (15).

5 Conclusions

A model of the grinding force of the AUPG of Zerodur was developed, taking into consideration the axial UV and the removal mechanism of the brittle material. AUPG and CG experiments were performed to validate the predictions of the grinding force model and analyse the effects of the axial UV on the grinding quality. The effects of the grinding parameters on the grinding force and Ra were also investigated for an industrial grinding process. Following are the conclusions drawn from the study:

1. The axial UV parallel to the grinding surface directly affects the motion of the individual abrasive grits, as well as the material performance and frictional force.
2. The predictions of the proposed grinding force model indicate that the grinding force decreases with increasing spindle speed, whereas it increases with increasing feed rate, grinding depth and grinding width.
3. The differences between the predictions of the proposed model and experimental measurements are 7.37 and 11.53% for the normal and tangential grinding forces, respectively.
4. Compared with CG, AUPG reduces the grinding force and improves the surface quality and form accuracy; the normal and tangential grinding forces are reduced by 27.31 and 22.52%, respectively, and the surface roughness by approximately 18.00%.
5. The proposed grinding force model is only applicable to the axial ultrasonic vibration-assisted peripheral precision grinding of Zerodur using a fine diamond grinding wheel. It, however, affords a basis for developing similar models for the AUPG and CG of other brittle materials.

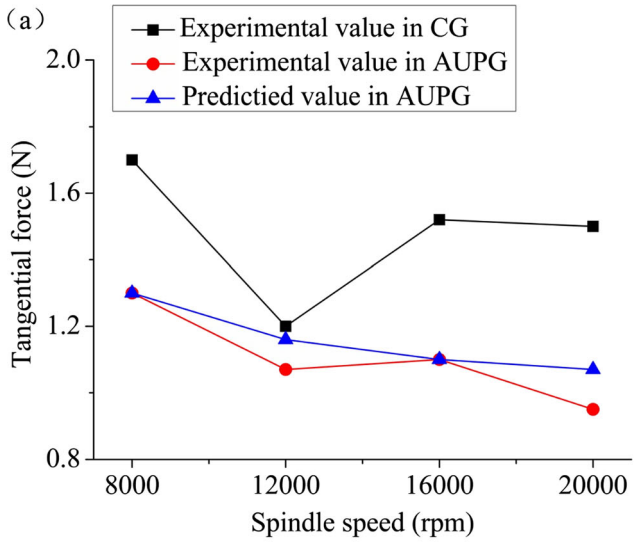

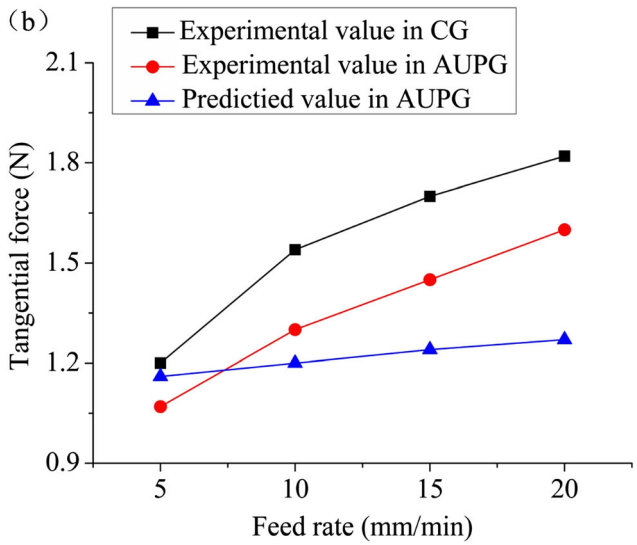

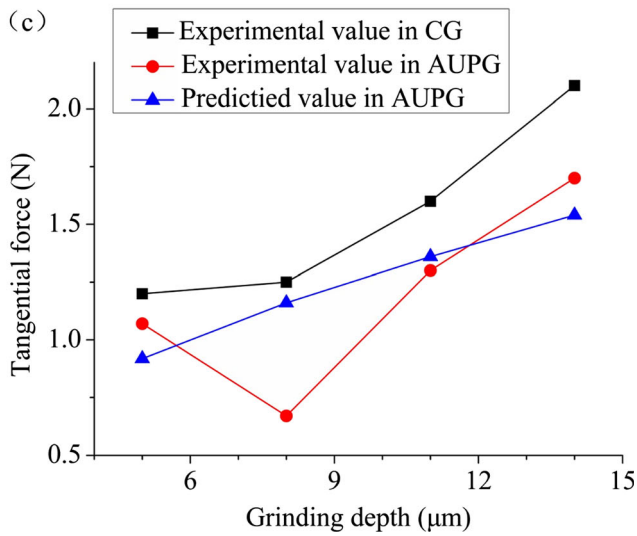

◀ **Fig. 17** Predicted and measured tangential grinding forces for **a** a_e = 8 μm, v_w = 5 mm/min; **b** a_e = 8 μm, n = 10,000 rpm; and **c** v_w = 5 mm/min, n = 10,000 rpm

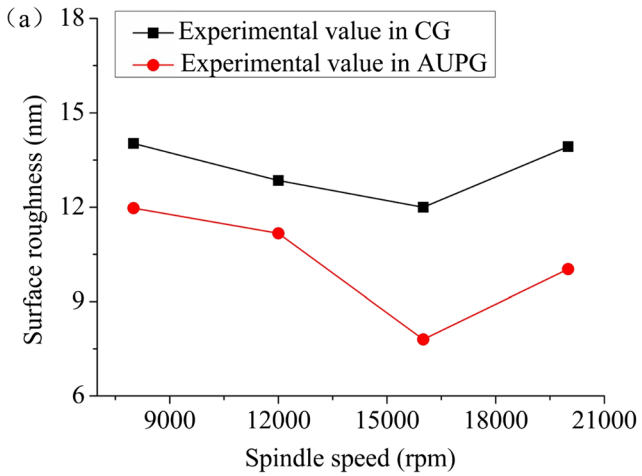

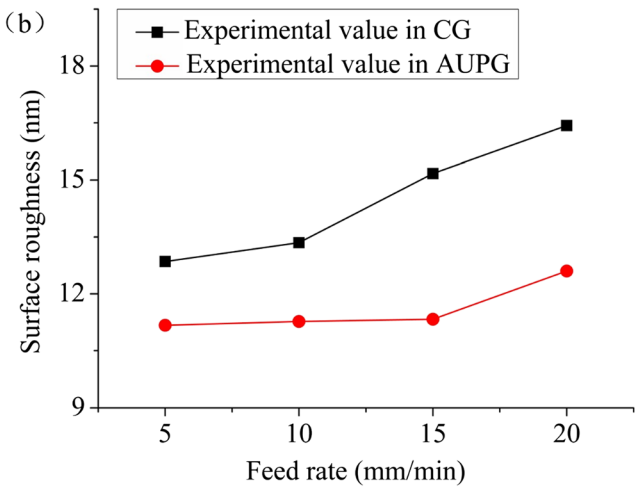

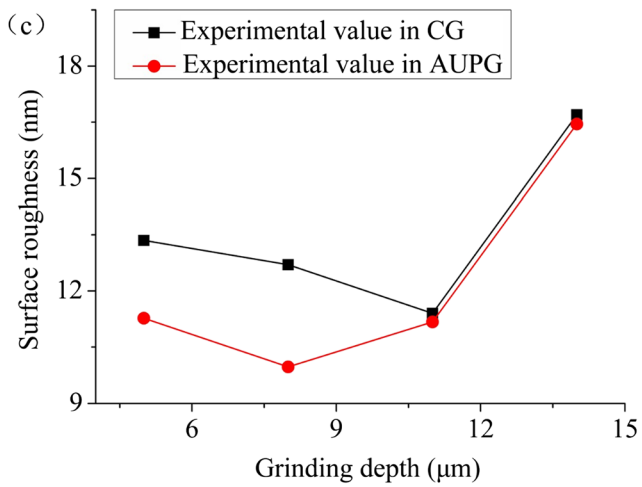

Fig. 18 Measured surface roughness for **a** a_e = 8 μm, v_w = 5 mm/min; **b** a_e = 8 μm, n = 10,000 rpm; and **c** v_w = 5 mm/min, n = 10,000 rpm

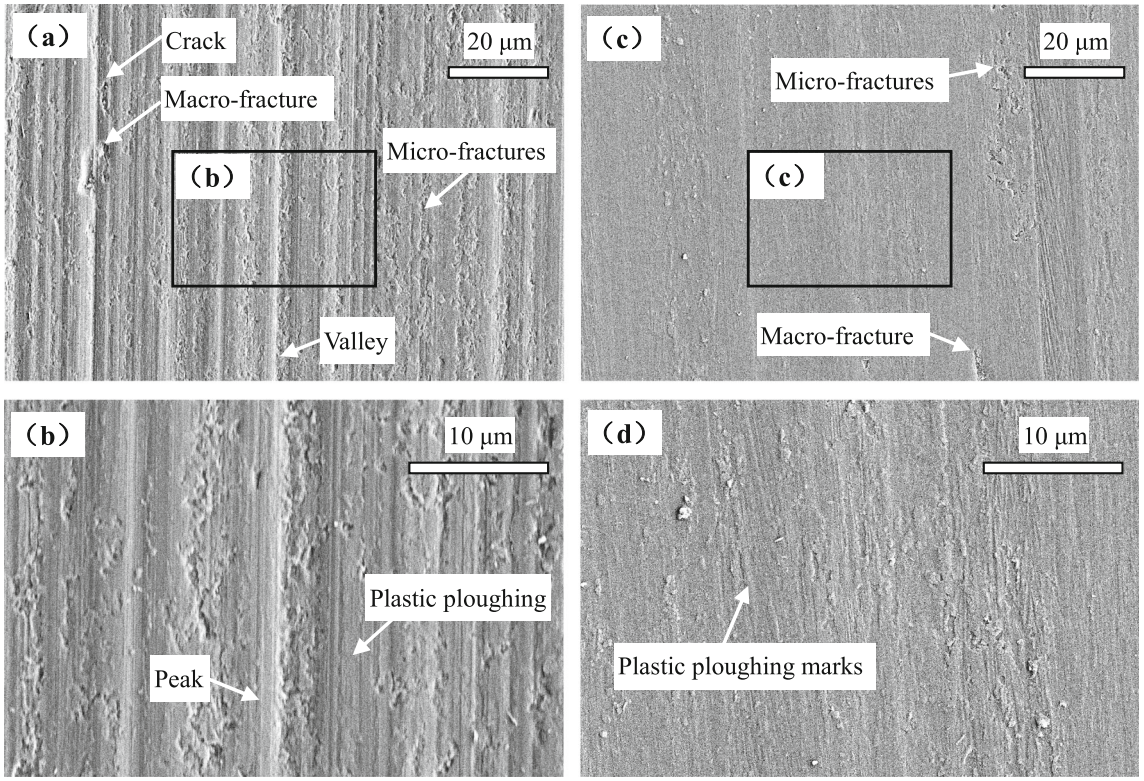

Fig. 19 Surface topographies observed by scanning electron microscopy after **a** CG, **b** CG, **c** AUPG and **d** AUPG in group 1 experiments

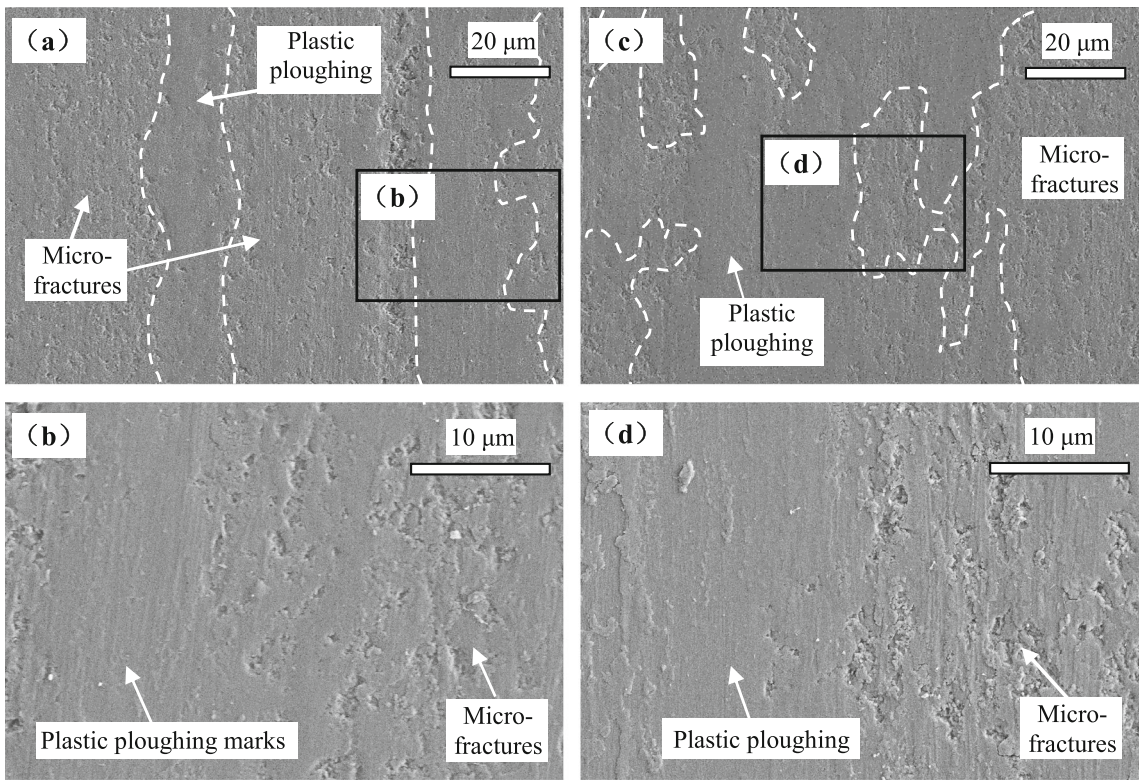

Fig. 20 Surface topographies observed by scanning electron microscopy after **a** CG, **b** CG, **c** AUPG and **d** AUPG in group 8 experiments

Funding This work was supported by National Natural Science Foundation of China (NSFC) (51475109), Youth Foundation of China (51402351) and Shandong Provincial Natural Science Foundation (ZR2014EEP025).

References

1. Wang Y, Lin B, Wang SL, Cao XY (2014) Study on the system matching of ultrasonic vibration assisted grinding for hard and brittle materials processing. Int J Mach Tools Manuf 77:66–73
2. Lv DX (2014) High frequency vibration effects in rotary ultrasonic machining hard-brittle material. Dissertation, Harbin institute of Technology
3. Cao JG, Wu YB, Fujimoto M, Nomura M (2014) Material removal behavior in ultrasonic-assisted scratching of SiC ceramics with a single diamond tool. Int J Mach Tools Manuf 79:49–61
4. Li SS, Wu YB, Fujimoto M, Nomura M (2016) Improving the working surface condition of electroplated cubic boron nitride grinding quill in surface grinding of Inconel 718 by the assistance of ultrasonic vibration. J Manuf Sci Eng 138:1–8
5. Ding K, Fu Y, Su HH, Xu HX, Cui FF, Li QL (2017) Experimental studies on matching performance of grinding and vibration parameters in ultrasonic assisted grinding of SiC ceramics. Int J Adv Manuf Technol 88:2527–2535
6. Peng Y, Liang Z, Wu Y, Guo Y, Wang C (2012) Characteristics of chip generation by vertical elliptic ultrasonic vibration-assisted grinding of brittle materials. Int J Adv Manuf Technol 62:563–568
7. Marinescu LD, Hitchiner M, Uhlmann E, Rowe WB, Inasaki I (2007) Handbook of machining with grinding wheels. Taylor & Francis Group, New York
8. Fujimoto M, Wu YB, Kanai H, Masahiko J (2013) Grinding characteristics of mould steel with micro 3D structure in ultrasonically assisted precision grinding. Int J Nanomanufacturing 9:201–210
9. Cao JG, Wu YB, Lu D, Fujimoto M, Nomura M (2014) Fundamental machining characteristics of ultrasonic assisted internal grinding of SiC ceramics. Mater Manuf Process 29:557–563
10. Qin N, Pei ZJ, Cong WL, Treadwell C, Guo DM (2011) Ultrasonic-vibration-assisted grinding brittle materials: a mechanistic model for cutting force, Proceedings of the ASME 2011 International Manufacturing Science and Engineering Conference MSEC 2011 June:13–17
11. Liu DF, Cong WL, Pei ZJ, Tang YJ (2012) A cutting force model for rotary ultrasonic machining of brittle materials. Int J Mach Tools Manuf 52:77–84
12. Liu SL, Chen T, Wu CQ (2017) Rotary ultrasonic face grinding of carbon fiber reinforced plastic (CFRP): a study on cutting force model. Int J Adv Manuf Technol 89:847–856
13. Zhang CG, Zhang JF, Feng PF (2013) Mathematical model for cutting force in rotary ultrasonic face milling of brittle materials. Int J Adv Manuf Technol 69:161–170
14. Xiao XZ, Zheng K, Liao WH (2014) Theoretical model for cutting force in rotary milling of dental zirconia ceramics. Int J Adv Manuf Technol 75:1263–1277
15. Zhang JH, Li H, Zhang ML, Zhao Y, Wang LY (2017) Study on force modeling considering size effect in ultrasonic-assisted micro-end grinding of silica glass and Al2O3 ceramic. Int J Adv Manuf Technol 89:1173–1192
16. Li C, Zhang FH, Meng BB, Liu LF, Rao XS (2017) Material removal mechanism and grinding force modelling of ultrasonicvibration assisted grinding for SiC ceramics. Ceram Int 43:2981–2930
17. Zhou M, Zheng W (2016) A model for grinding forces prediction in ultrasonic vibration assisted grinding of SiCp/Al composites. Int J Adv Manuf Technol 87:3211–3224
18. Xiao XZ, Zheng K, Liao WH, Meng H (2016) Study on cutting force model in ultrasonic vibration assisted side grinding of zirconia ceramics. Int. J. Mach. Tools Manuf 104:58–67
19. Kumar VC, Hutchings IM (2004) Reduction of the sliding friction of metals by the application of longitudinal or transverse ultrasonic vibration. Tribol Int 37:833–840
20. Tsai CC, Tseng CH (2006) The effect of friction reduction in the presence of in-plan vibrations. Arch Appl Mech 75:164–176
21. Chen MJ, Zhao QL, Dong S, Li D (2005) The critical conditions of brittle–ductile transition and the factors influencing the surface quality of brittle materials in ultra-precision grinding. J Mater Process Technol 168:75–82
22. Hecker RL, Liang SY (2003) Predictive modeling of surface roughness in grinding. Int J Mach Tools Manuf 43:755–761
23. Wu CJ, Li BZ, Liu Y, Liang SY (2017) Surface roughness modeling for grinding of silicon carbide ceramics considering co-existence of brittleness and ductility. Int J Mech Sci 133:167–177
24. Durgumahanti USP, Singh V, Rao PV (2010) A new model for grinding force prediction and analysis. Int J Mach Tools Manuf 50:231–240
25. Wu CJ, Li BZ, Yang JG, Liang SY (2016) Prediction of grinding force for brittle materials considering co-existing of ductility and brittleness. Int J Adv Manuf Technol 87:1967–1975
26. Peng Y, Liang Z, Wu Y, Guo Y, Wang C (2012) Effect of vibration on surface and tool wear in ultrasonic vibration-assisted scratching of brittle materials. Int J Adv Manuf Technol 59:67–72